Nano Energy 58 (2019) 842–851

Contents lists available at ScienceDirect

Nano Energy

journal homepage: www.elsevier.com/locate/nanoen

Full paper

Conformal fluorine coated carbon paper for an energy harvesting water wheel

Dongyue Jiang[a,*], Fei Guo[a], Minyi Xu[b,*], Jingcheng Cai[a], Shuo Cong[a], Ming Jia[a], Guijun Chen[a], Yongchen Song[a]

[a] Key Laboratory of Ocean Energy Utilization and Energy Conservation of Ministry of Education, Dalian University of Technology, 116024, China
[b] Marine Engineering College, Dalian Maritime University, Liaoning Province 116026, China

ARTICLE INFO

Keywords:
TENG
Water wheel
Energy harvesting
Superhydrophobic

ABSTRACT

Utilizing the kinetic energy of a flowing river for irrigation could be tracked back to Hellenistic and Roman periods. In modern days, hydroelectric plants are built for harvesting the kinetic energy of the flowing river. However, a large investment is required in the hydroelectric plants for maximizing the power output. Here we present a low-cost and scalable TENG (triboelectric nanogenerators) based energy harvesting water wheel (ww-TENG). The water wheel works in a sliding freestanding TENG mode which generates power from the charges flow induced by contact electrification and electrostatic induction. A conformal fluorine coated carbon paper (f-CP) was employed to form the alternate electrodes. The deposited fluorine layer provides the benefits of high affinity to attract electrons as well as hydrophobicity for water repelling. The carbon paper offers a high electrical conductivity and rough structure to form a superhydrophobic property. These features enables a large charge induction and fast water/TENG separation for maximizing the power output of the energy harvesting water wheel. A lab-scale water wheel (diameter 10 cm and width 2.5 cm) is fabricated and a maximum 5.3 μW output power was measured under 50 MΩ resistance at a linear flow velocity of 2.6 m/s. The ww-TENG was employed for charging a 10 μF capacitor to 16 V and lighting up a commercial LED light bulb. As a comparison, an electromagnetic generator (EMG) could only charge the capacitor to 2.7 V with the same period of time. The EMG obtains a high power output at low load resistance case (< 100 kΩ) while the ww-TENG generates high power when the load resistance is large (> 10 MΩ). The present ww-TENG shows great potential for harvesting the kinetic energy from flowing river and targets for the applications with large load resistance like electrostatic systems.

1. Introduction

Water wheels have been used as irrigation tools and power sources since Hellenistic and Roman periods. They were widely employed to save the labors in ancient times [1–3]. Diverse devices were created such as water mills, paddle wheel warships, and even Puppet Theater by employing the mechanical energy from the flowing water. In modern days, water wheels are broadly used together with an electromagnetic generator to convert mechanical energy from water flow to electricity. Water turbine based power plants (hydroelectric power plants) are launched to supply electricity to the power grid. As compared to other types of power plants (combustion based or nuclear power plants), the water turbine based power plant show good potential because they are environmentally friendly with zero emission. However, the river flow velocity is typically slow (ranging from 0.05 to 3 m/s [4–6]). A direct conversion from the water flow energy into electricity by electromagnetic generators could not be incorporated in the power network. In order to maximize the power output of a hydroelectric power plant, large investment should be conducted to construct a dam for increasing the potential energy of water. This significantly increases the cost and complexity of a hydroelectric plant, and thus limits the popularization of this technology.

In recent years, triboelectric nanogenerators (TENG) have been widely studied since the first report in 2012 by Prof. Zhong Lin Wang's group [7–9]. Different from the electromagnetic power generators which drives electron flow (electricity) via Lorentz force, TENG mainly utilizes the displacement current induced by the time-varying electric field and polarization field [10–12]. This ensures a high power output for TENG when harvesting the low frequency mechanical energy which is less efficient in electromagnetic power generators [13–18]. This

* Corresponding authors.
E-mail addresses: jiangdy@dlut.edu.cn (D. Jiang), xuminyi@dlmu.edu.cn (M. Xu).

https://doi.org/10.1016/j.nanoen.2019.01.083
Received 20 December 2018; Received in revised form 17 January 2019; Accepted 18 January 2019
Available online 01 February 2019

feature of TENG opens up an opportunity for direct harvesting the low speed water flow energy in a cost-effective way. Water contact and separation based TENGs are demonstrated for harvesting the energy from water droplet, wave, water fall and blue energy from ocean [19–33]. The demonstration of a sliding freestanding mode TENG for harvesting river flow energy would be highly desired. Considering the large cost and complexity of an electromagnetic type hydroelectric plant, here we report a low-cost, scalable water wheel triboelectric nanogenerator (ww-TENG) for harvesting the low speed water flow energy directly.

In a sliding freestanding mode water TENG device, the output power is proportional to the variation of the induced charge density with respect to time. As a result, a large charge induction within a short period of time is essential for achieving high output power. However, due to the existence of the adhesion force when water is interacting with a solid surface, the separation typically happens in a sluggish manner, which has been proved to reduce the output performance of a hand-driven water-TENG [28]. In this study, a conformal fluorine coated carbon paper is proposed for boosting the performance of the ww-TENG. Firstly, carbon paper has been widely employed as the electrode for flow batteries, Lithium-ion batteries and TENG devices due to its high electrical conductivity, flexibility and large contact area [34–36]. Besides, the carbon paper could also provide a rough surface structure for obtaining a superhydrophobic property [37] which is desired in the ww-TENG. Fluorine is employed as the coating material on the carbon paper because of its high affinity of negative charges when in contact with water as well as its hydrophobicity. Integrating the advantages provided by fluorine and carbon paper, a ww-TENG device is developed for harvesting the low speed flow energy. This presented ww-TENG is half immersed in a flowing river and driven by the continuous water flow. The flow motion of the river induces a rotation of the ww-TENG, thus the fluorinated carbon paper surface alternatively contact and separate with the water. With a triboelectrification effect, the charges are accumulated on the fluorinated carbon paper in sequence and an AC type signal could be detected. This present ww-TENG offers the advantages of: i) utilizing the charges flow induced by the contact electrification and electrostatic induction which allows for a power generation even in the low speed rivers; ii) the employed fluorinated carbon paper enables a fast separation between water and TENG surface, which is essential for the output performance of ww-TENG; and iii) this ww-TENG could be used either by its alone, or together with a conventional electromagnetic generator to boost the power output. Detailed results and discussions on the effects of electrode size, rotating speed, ions and pH condition in the water are carried out.

2. Working principle and methods

Fig. 1a shows the concept of a ww-TENG, which is composed of a water wheel, a shaft for supporting and fixing the water wheel, paddles for repelling water, alternate carbon paper electrodes and hydrophobic fluorine coating. The electrodes are alternatively connected and the two output terminals are connected with the external circuit for measurement. During operation, the ww-TENG is partially immersed in a flowing river as shown in Fig. 1a, with the effect of paddles, the water flow rotates the ww-TENG. The working principle is explained in Fig. 1b. Stage I: the whole fluorine coating attains negative charges when the ww-TENG is rotating in the water and the charges would not dissipate in an extended period of time [22]. Only the negative charges close to the red and blue electrodes are illustrated as they are affecting the current flow during the triboelectrification process. Initially, the red and blue electrodes are in electrical equilibrium and no current signal could be detected as shown in the inset image at stage I. Stage II: when the red electrode is driven to be immerged in the water, an interfacial electrical double layer (EDL) is formed and the negative triboelectric charges on the fluorine layer are screened by the positive charges in the water. Due to the unbalanced electric potential between red and blue electrodes, free electrons are driven from blue electrode to the red electrode, thus a current signal with the direction from red electrode to the blue electrode (defined as positive) could be detected. Stage III:

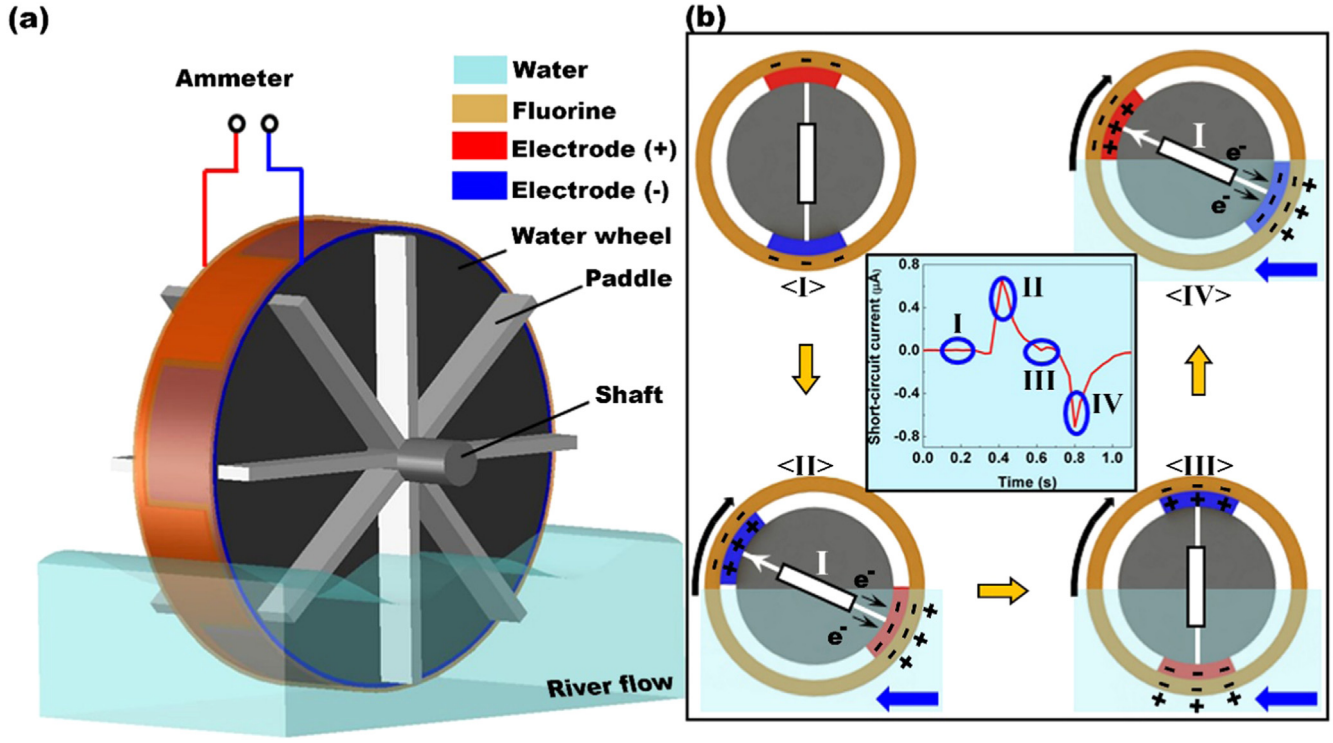

Fig. 1. (a) Schematic of the ww-TENG, which is composed of a water wheel, 8 paddles on each side, a shaft, alternate electrodes and fluorine layer. The ww-TENG is immersed and rotated by flowing river. (b) The working principle of the ww-TENG during the rotating process and the output short-circuit current.

with a further rotation induced by the river flow, the red electrode is rotating in the water and the blue electrode is moving in the air. There is no further asymmetric screening of the negative charges and no current could be generated. This could be represented by the zero output zone (stage III) in the inset image. Stage IV: when the red electrode emerges and the blue electrode gets immerged, a same process of stage II is repeated and the electron flow is driven by the unbalanced electric potential from red electrode to blue electrode, thus a current with the direction from blue to red electrode (defined as negative) could be generated. Further rotating motion could be represented by the cycle from stage II to stage IV.

In the present study, a water wheel (with paddles and center hole) is fabricated by 3D printing, the diameter and width of the water wheel are 100 mm and 25 mm, respectively. On each side of the water wheel, 8 paddles are attached to the water wheel with the size of 45 mm × 10 mm × 3 mm (Length × Width × Height). At the center of the water wheel, a hole with a diameter of 10 mm is designed for shaft and bearing to support and fix the water wheel. As the water wheel surface is in a curved shape, ITO (indium tin oxide) coated PET (polyethylene terephthalate) film is employed to form the alternate electrodes. Fluorinated plain ITO (f-ITO) electrodes and fluorinated carbon paper (f-CP) electrodes were prepared for comparison in Section 3.2. The f-ITO electrodes were prepared by directly depositing fluorine on the plain ITO electrodes in an iCVD (Initiated Chemical Vapor Deposition) reactor. The fluorinated carbon paper electrodes (f-CP) were obtained by two steps. Firstly, a piece of as purchased carbon paper (Toray TGP-H-60) was tailored and attached to the flexible ITO electrode by conductive epoxy. Secondly, a conformal fluorine deposition was conducted by iCVD reactor. 1 H,1 H,2 H,2H-Perfluorodecyl acrylate (PFDA) monomer (97%) was obtained from Sigma-Aldrich. The PFDA monomer was vaporized and delivered into the reactor through a steel capillary tube. The t-butyl peroxide initiator (97%, Shanghai Aladdin Bio-Chem Technology Co., LTD) was fed into the chamber at the flow rate of 0.1 mL/min. The carbon paper was placed on the bottom of the chamber and the deposition process was maintained for one hour. The morphologies (taken by FEI Inspect F50) of the untreated carbon paper and fluorine coated carbon paper could be seen in Fig. 2a and b. The scale bar in the figure indicates a length of 50 μm. As the deposited fluorine layer is very thin (~ 10 nm), there is no clear difference in morphology (except for a smoother surface on the f-CP surface) between the untreated and fluorine coated carbon paper. The images with higher resolution of untreated CP and f-CP could be found from Supporting information (Fig. S1). A XPS (X-ray photoelectron spectroscopy, ESCALAB 250Xi) test is conducted between the untreated CP and the f-CP electrodes. Fig. 2c shows the survey spectrum of the untreated CP sample and a very high carbon C1s peak could be observed. This result indicates that the major element in the untreated electrode is carbon. As a comparison, the survey spectrum of the f-CP sample is shown in Fig. 2d. It is seen that the percentage of C1s reduces to 38.5% and fluorine increases to 61.5%. Fig. 2e and f present the narrow scan of the C1s peaks of the two samples. Only C-C could be observed in the untreated CP sample, while C-C, C-O, O-C=O, CF, CF_2 and CF_3 peaks could be seen in the whole spectrum. Detailed composition of the CP and f-CP samples could be seen in Supporting information, Table S1. It is noteworthy that the formation of C-O and O-C=O could be formed during the iCVD deposition process. This result could prove the existence of fluorine on the CP surface. The insets of Fig. 2e and f show a water droplet (2.5 μL) contact angle test on the untreated carbon paper electrode as well as on the fluorinated carbon paper electrode. It is seen that a very large water contact angle (153°) is obtained on the fluorinated carbon paper electrode, as compared to the untreated carbon paper electrode (111°). This is because the fluorine possesses a very low surface energy and prevents the water droplet penetrating into the air pockets of the f-CP. The prepared water wheel with f-CP electrode is shown in the inset of Fig. 2f. During measurement, the prepared water wheel is half immersed in the flowing water. The motion of the water wheel is captured by a high speed camera (Photron FASTCAM UX100) and the frame rate is set as 2000 fps. The output current signal are measured by a Keithley 6514 electrometer. As the electrodes on the ww-TENG are rotating, a slip ring was employed for connecting the rotating electrodes to the fixed terminals of the electrometer. In a control experiment to quantify the effect of rotating speed of the ww-TENG, a step-motor was employed to provide a constant rotating speed.

3. Results and discussion

In order to evaluate the performance of the ww-TENG, experimental tests are conducted to study the effect of the electrode size, number, and the effects of ww-TENG rotating speed, ion/pH property of the water. The recorded short-circuit current and output power are compared under different working conditions. Load resistors with different resistance (1 MΩ–1 GΩ) are used to pursue a maximum power.

3.1. Effect of electrode size

Here we present the effect of electrode size on the power output of the ww-TENG. In this section, f-ITO electrodes are employed for studying the output characteristics of the ww-TENG. Firstly, a pair of short electrodes with the dimension of L40 mm × W25 mm is used. The two electrodes are placed symmetrically on the ww-TENG, and the gap between the two electrodes is kept as 117 mm. The ww-TENG is half immersed in a container which is filled with tap water. The tap water is with pH value of 7.2, electrical conductivity of 310 μS/cm and TDS (total dissolvable solids) 123 mg/L. In order to keep a constant rotating speed, a step motor is employed to drive the ww-TENG device. A slow rotating speed (75 rpm, linear speed 0.39 m/s) is employed for reducing the adverse effect caused by the dragged water at high rotating speed. Fig. 3 presents the short-circuit current, open-circuit voltage and transferred charges varying with the electrode length. In Fig. 3a, when one electrode is immersed in the water, the triboelectrification phenomena happens and induces a current flow, thus a peak current of 0.75 μA is measured by the electrometer. When the electrode emerges from the water, the other electrode starts immersing in the water, which leads to a negative current signal. It is noteworthy that due to the existence of the gap between the two electrodes, a close to zero output signal (inset of Fig. 3a) could be observed between the positive and negative peaks. This happens when one electrode is fully immersed in the water and the other is exposed in the air. It is seen that the duration of the zero output signal is not as long as the gap between the two electrodes. This could be attributed to the residual water adhered on the electrodes. The residual water is dragged by the adhesion force between water and electrode surface even when the electrode is rotated above the water level. A detailed discussion on the water adhesion could be found in Section 3.2. As compared to the short electrodes, a pair of long electrodes is prepared with the dimension of L140 mm × W25 mm, two gaps with the length of 17 mm are between the electrodes. The short-circuit current is shown in Fig. 3b. It is seen the magnitude of the current is the similar with the short electrode. This is because the output current ($I \propto A\frac{d\sigma_I}{dt}$, I is the current, A is the contact area, $d\sigma_I/dt$ is the induced charge density with respect to time) is proportional to the variation of the induced surface charge with respect to time. The rotating speed and width of the electrodes are the same for both the short and long electrodes, which yields a similar variation of charge induction at a certain time. For the ww-TENG with a long f-ITO electrode, the zero output signal could not be detected between the positive and negative peaks. However, a plateau signal with fluctuation appears at positive and negative zones. This plateau zone is caused by the continuous immerging and emerging of the two fluorinated electrodes alternatively. The fluctuation could be caused by the unstable water motion during the rotating of ww-TENG. By increasing the electrode length, the energy density of the ww-TENG device could be increased.

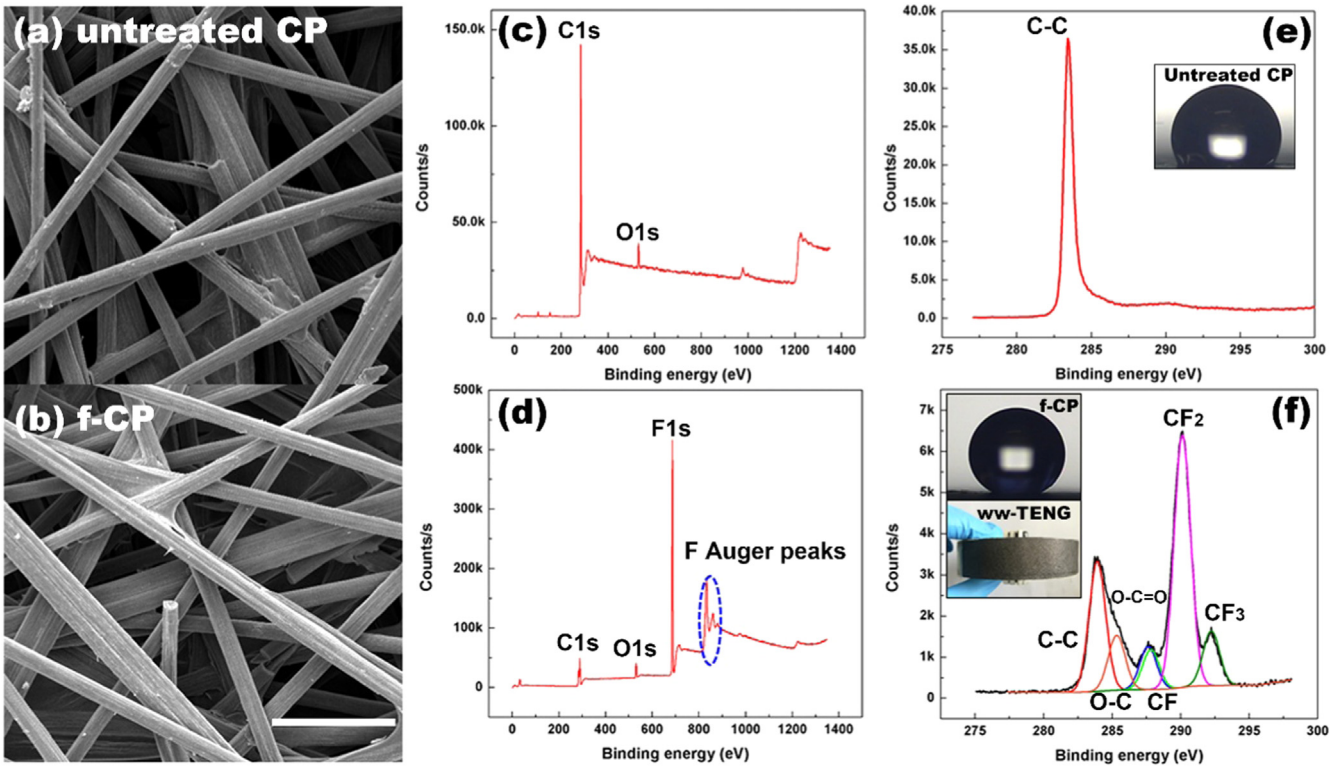

Fig. 2. SEM morphologies of the (a) untreated carbon paper and (b) fluorinated carbon paper, the scale bar in (a) and (b) indicates a length of 50 μm. (c-d) The survey scan of the untreated CP and f-CP sample under XPS characterization. (e-f) The narrow scan of the C1s peak of the CP and f-CP samples. Insets of (e) and (f) show the water contact angle test of a 2.5 μL droplet on the untreated CP sample (e) and f-CP sample (f). The fabricated ww-TENG with f-CP is shown in the inset of (f).

The open-circuit voltage of the ww-TENG with short and long electrodes are measured and shown in Fig. 3c and d. As the electrons could not transfer during an open-circuit condition, the V_{oc} here is defined as the electric potential between the red and blue electrodes. An average ~ 8 V peak-to-peak open-circuit voltage could be obtained when the rotating speed is 75 rpm, which corresponds to a linear sliding speed of 0.39 m/s. Fig. 3e and f present the transferred charges during the rotating motion of ww-TENG. During one cycle rotation, an average transferred charge of ~ 40 nC was reached by the short electrodes. With the increase of the electrode length, the average transferred charge during one cycle could be over 110 nC. The more charges induced by the pair of long electrodes are comparable with the larger average short-circuit current as shown in Fig. 3b.

The effect on the number of electrode pairs is investigated. Three ww-TENG devices with 1, 2 and 3 pairs of short electrodes (L = 40 mm) are prepared. Fig. 4a presents a continuous measurement of the short-circuit current with two pairs of electrodes. It is seen that the magnitude of the short-circuit current is the same with that obtained by single pair of electrodes. However, as shown in the inset of Fig. 4a, there exists dual peak and trough values in one cycle, which are induced by the two pairs of electrodes. The average short-circuit current in one rotation cycle obtained by the three ww-TENG devices are calculated. As shown in Fig. 4b, the ww-TENG device with single pair of electrodes possesses smallest average current, which could be attributed to the zero signal zones as presented in Fig. 3a. With the increase of electrode pair numbers, the average current increases in a linear trend. A 0.46 μA average short-circuit current in one rotation cycle is obtained when three pairs of short electrodes are employed. This value is closed to the average short-circuit current obtained by single pair of long electrodes (L = 140 mm).

3.2. Effect of rotating speed

In this section, the effect of the rotating speed of ww-TENG has been examined. The electrode length is kept as L = 140 mm for its higher output performance without the zero output signal zone. By changing the rotating speed of the step motor, the ww-TENG was driven at speeds from 75 to 500 rpm. An average peak current is employed for comparing the performance of the ww-TENG at varying rotating speeds. The average peak current is calculated based on 20 data points. As shown in Fig. 5a, the average peak current increases initially with the increase of the rotating speed from 75 to 300 rpm. This could be expected as the current is proportional to the variation of induced charges with respect of time. However, when the rotating speed is above 300 rpm, a decreasing trend could be observed. A similar trend was obtained in a hand-driven water rotating wheel [28]. In order to examine the mechanism of this phenomena, a high speed camera is employed to study the water dynamics on the f-ITO surface at different rotating speed. Initially, the ww-TENG is half immersed in the water and the water adhered to the f-ITO surface. With the rotation of the ww-TENG, the adhesion force between water and ww-TENG drag the water climbing above the water level. As shown in Fig. 5b-d, the amount of water dragged by the ww-TENG with a pair of f-ITO electrodes increases with the rotating speed. When the rotating speed reaches 500 rpm, the water could be dragged to the top end of the ww-TENG. Such a contact between water and f-ITO surface prevents a fast separation and leads to a reduction in the output performance of the ww-TENG. As a comparison, the ww-TENG with a pair of f-CP electrodes is tested. As shown in Fig. 5e-g, the amount of dragged water also increases with the rotating speed. However, this is significantly reduced as compared to the amount of water dragged by the f-ITO electrodes. This is because that the f-CP electrode possesses a much lower surface energy, which is favorable for a fast separation between water and ww-TENG surface. As a result, the average peak current keeps increasing with rotating speed

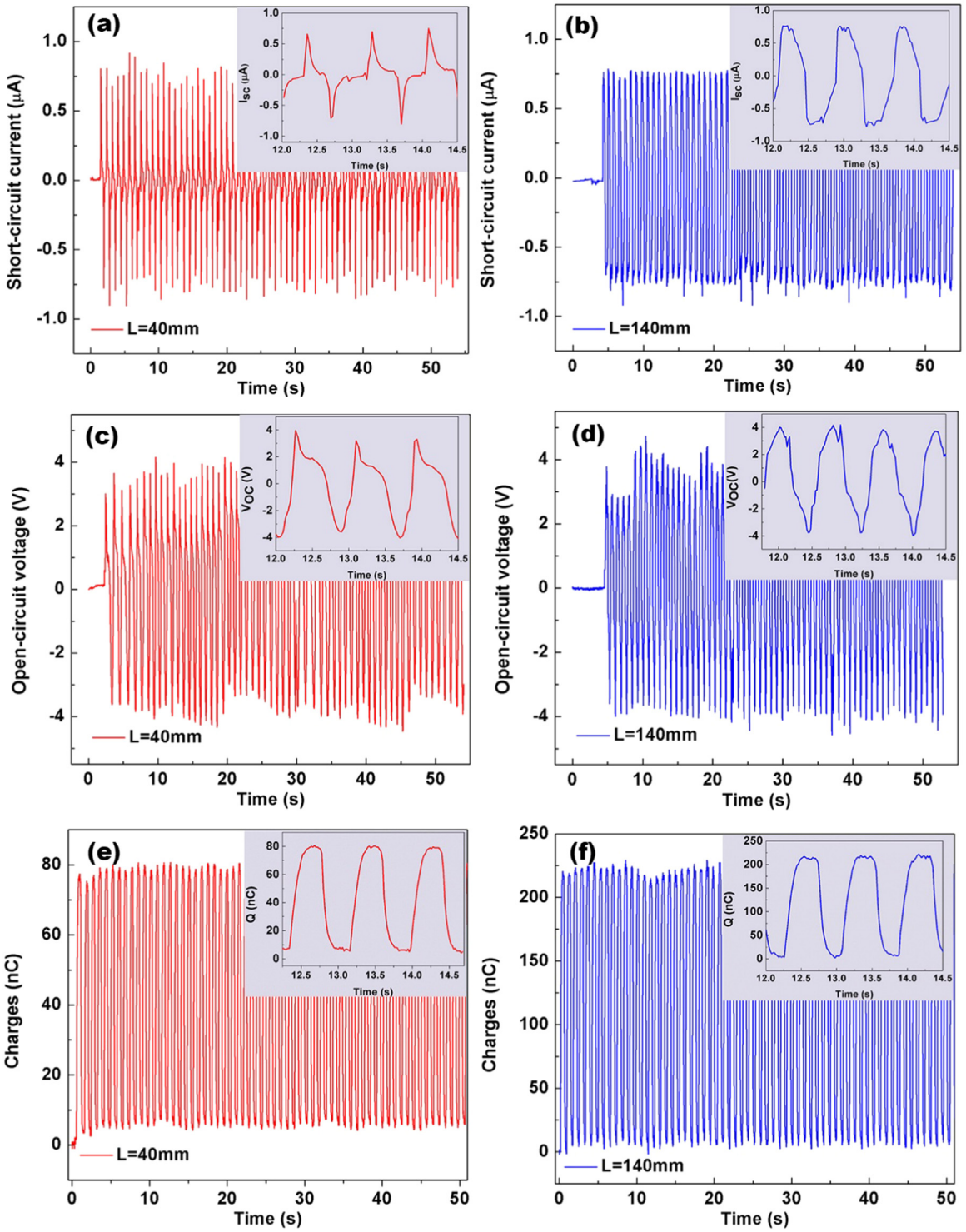

Fig. 3. Output performance of ww-TENG: (a-b) Short-circuit current obtained with a pair of short (L = 40 mm) and long (L = 140 mm) f-ITO electrodes. (c-d) Open-circuit voltage obtained with a pair of short (L = 40 mm) and long (L = 140 mm) f-ITO electrodes. (e-f) Transferred charges obtained by a pair of short (L = 40 mm) and long (L = 140 mm) f-ITO electrodes.

as shown in Fig. 5a. A movie clip showing the water dragged by the rotating ww-TENG could be found in the Supporting information. A further increase in the rotating speed would lead to the reduction of average peak current. This is because the other components of the ww-TENG such as sticking tapes, and connecting do not possess the superhydrophobic property and make adverse effects to the average peak current.

Fig. 5 presents the high speed camera captured images of the water dynamics interacting with different electrodes. An analysis on this phenomena is carried out in this section. The water is continuum during the contact and drag motion. The interaction between the ww-TENG, water and air involves a multiphase flow process with a rotating wall. Fig. 6a presents the force analysis of the water in contact with the surface of the ww-TENG. When the ww-TENG starts rotating, the water undertakes gravitational force and the adhesion force. When the gravitational force is greater than the vertical component of the adhesion

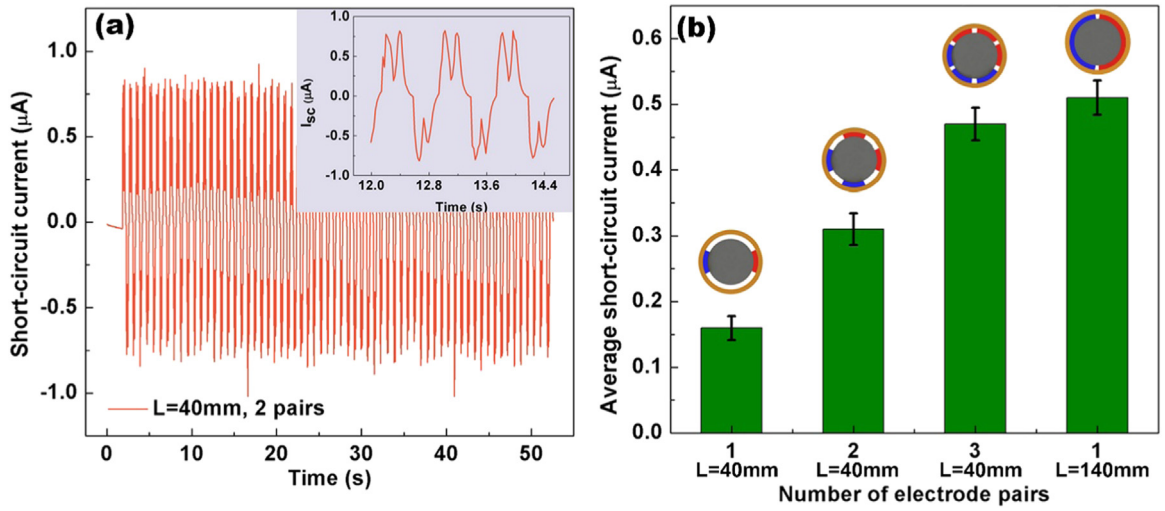

Fig. 4. (a) Short-circuit current of ww-TENG with 2 pairs of short (L = 40 mm) f-ITO electrodes. (b) Average peak current obtained with 1, 2 and 3 pairs of short (L = 40 mm) and one pair of long (L = 140 mm) f-ITO electrodes.

force, the water would separate from the surface ($F_G > F_{ad}\cos(\theta_i)$, θ_i is the angle between the direction of adhesion force and vertical). The adhesion force could be evaluated by Eq. (1):

$$F_{ad} = kL\gamma(\cos\theta_{adv} - \cos\theta_{rec}) \quad (1)$$

where k is the dimensionless factor which accounts for the precise shape of the solid-liquid-air three phase contact line. It could be calculated based on ref. [38]. L is a length scale representing the contact line of the dragged water. γ is the interfacial tension between liquid and air. θ_{adv} and θ_{rec} are the advancing and receding contact angles of the fluid, respectively. It should be noted that the advancing contact angle is dependent on the rotating velocity of the ww-TENG [39]. In this study, the advancing contact angle is measured from the high speed camera captured images. As shown in Fig. 5b-g, the advancing contact angle θ_{adv} of the dragged water reduces with the increase of rotating speed and surface energy. As a result, a higher adhesion force could be obtained at higher rotating speed conditions, which is in agreement with the results presented in [40]. Based on Eq. (1), the calculated adhesion force is presented in Fig. 6b. The measured data points (dots) are obtained by measuring the gravitational force of the water which is dragged by the ww-TENG. A good agreement is achieved between the calculated and the measured data. The details of the measurement of the gravitational force could be found in Fig. S2 in the Supporting information. A finite element analysis (FEA) model demonstrating the interaction between the dragged water and the f-ITO as well as the f-CP electrodes was established. Laminar flow and phase field interfaces were employed in COMSOL Multiphysics for modelling the rotating and wetted wall. The measured equilibrium contact angles of 111° for f-ITO electrodes and 153° for f-CP electrodes were imported to the model. Fig. 6c-e present the amount of water dragged by the ww-TENG with f-ITO electrodes at the rotating speeds of 100, 300 and 500 rpm, while Fig. 6f-h show the dragged water by ww-TENG with a pair of f-CP electrodes. The red color legend represents the volume fraction of air. The simulated results match well with the experimental measurement as shown in Fig. 5b-g. The f-CP electrodes show better performance of water separate motion, as compared to the f-ITO electrodes.

3.3. Effects of ion concentration and pH value

Considering the working conditions of the ww-TENG, the ion and pH property of the flowing river should be taken into account. According to a measurement on the ion type and concentration in Yangtze River [41], the Na^+, Ca^{2+}, Cl^-, SO_4^- are with higher concentration as compared to other types of ions. NaCl, $CaCl_2$, Na_2SO_4, and

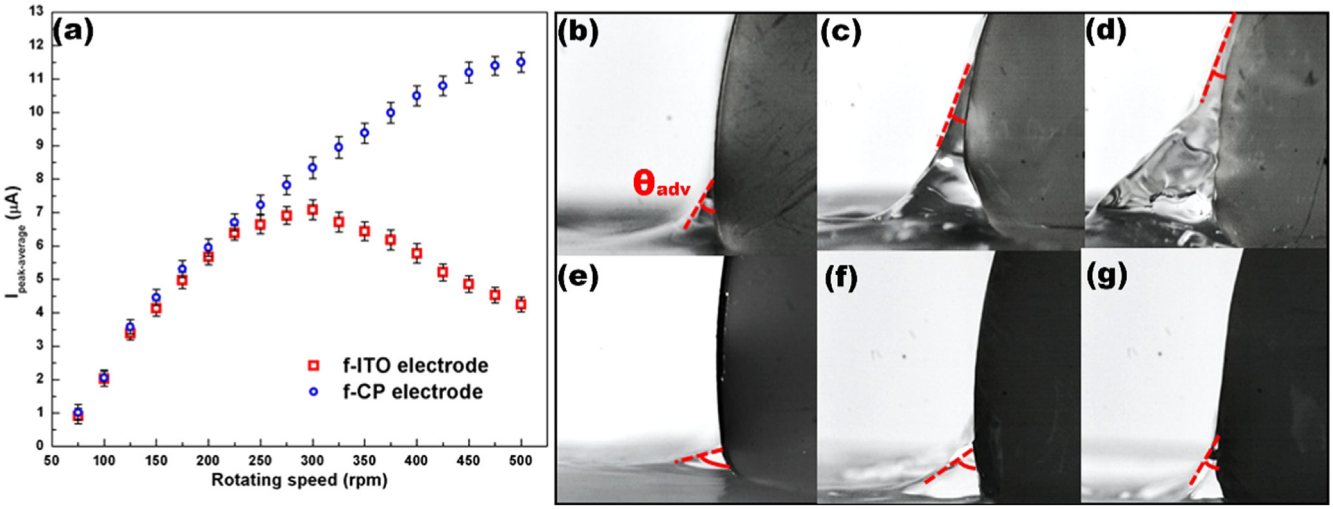

Fig. 5. (a) Comparisons of average peak short-circuit current obtained by f-ITO electrode and f-CP electrode, (b-d) Snapshots of water dragging by the ww-TENG with f-ITO electrode (100, 300 and 500 rpm, respectively), (e-g) Snapshots of water dragging by the ww-TENG with f-CP electrode (100, 300 and 500 rpm, respectively).

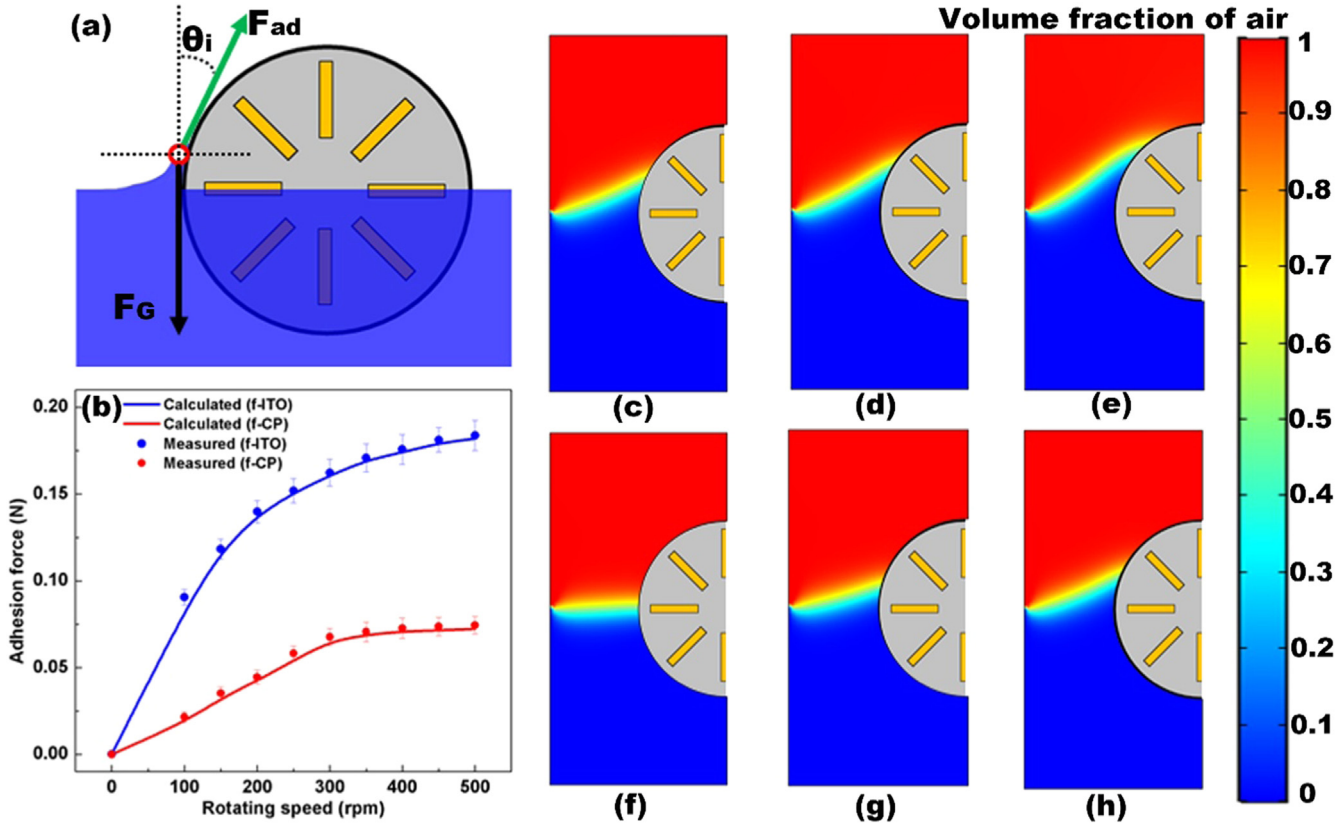

Fig. 6. (a) Force analysis of the dragged water in contact with the rotating ww-TENG and (b) Adhesion force of the f-ITO electrodes and f-CP electrodes. (c)-(e) The water/air interface induced by the ww-TENG with f-ITO electrodes at 100, 300 and 500 rpm, (f)-(h) The water/air interface induced by the ww-TENG with f-CP electrodes at 100, 300 and 500 rpm.

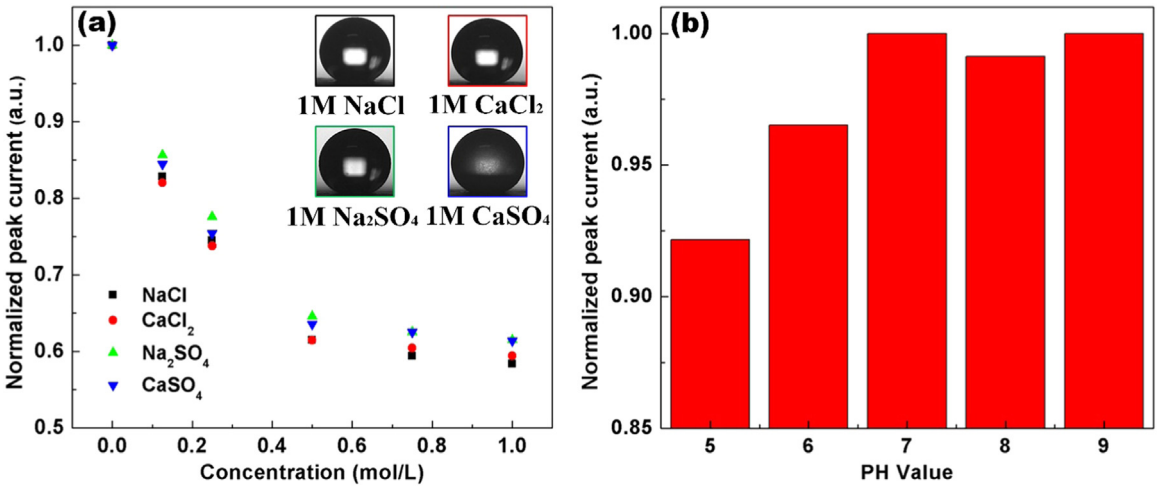

Fig. 7. (a) Effects of ion type and concentration on the normalized average peak short-circuit current. (b) Effects of PH value on the normalized average peak short-circuit current.

$CaSO_4$ solutions (0–1 mol/L) are prepared by mixing these salts into DI (deionized) water. As shown in Fig. 7a, a decreasing trend could be observed with the increase of the ion concentration. This could be attributed to the reduced amount of negative charges on the fluorine layer when electrolytes are added into the DI water [42]. The reduced amount of negative charges contributes less to the asymmetric screening of the charge movement and thus leads to a decreased current output. The contact angles of the above mentioned salt droplets (1 M) are measured. As shown in the inset of Fig. 7a, these droplets all preserve a very high contact angle over 150° as the f-CP possesses very low surface energy. Such a low surface energy eliminates the condition that the residual electrolyte solution sticking to the TENG surface and reducing the output performance [23]. It is noteworthy that the surface tension γ of the DI water is increased when inorganic salts are added (for example, DI water at 25 °C: 72 mN/m, 1 M $CaCl_2$ at 25 °C: 76 mN/m [43]), which would increase the adhesion force between the liquid and the ww-TENG surface according to Eq. (1). On the other hand, the addition of salts also increases the density of the solution (1 M $CaCl_2$:~ 1111 kg/m^3), which increases the gravitational force. As both the adhesion force and gravitational force increase, the variation of the

net force is less than 5% of the adhesion force (for example, 3 mN at 500 rpm). Such a small net force variation contributes less to the water dynamics. In terms of ions type, the output performance is influenced by the electronegativity and electrical conductivity of the ions [44]. Due to a similar electronegativity between Na^+ and Ca^{2+}, the average peak current of the two types of ions with the same anions are in the similar range. It is found that the average peak currents of the SO_4^{2-} anions are larger than that obtained by Cl^-. This is because the electrical conductivity of SO_4^{2-} is smaller than Cl^- and the output current is inversely proportional to the electrical conductivity of the solution. [45]. The pH value in the river is typically ranging from 6.5 to 9.0 [46]. Buffer solutions with the pH value ranging from 5.0 to 9.0 are prepared. As shown in Fig. 7b, the alkaline environment does not affect the average peak current of the ww-TENG. However, an acid environment would weaken the output performance. This is because the high concentration of the H^+ would render more cations in the water phase [47]. Thus the anions are not easy to pass through the interface and make the fluorine surface negatively charged (Supporting information in [42]).

3.4. Output performance of ww-TENG

In order to examine the output performance of the ww-TENG, a comparison is drawn between the presented ww-TENG and a commercial EMG (Zhuoye130). Both the ww-TENG and EMG are working at a speed of 500 rpm. It is noteworthy that the selection of the EMG is based on the output torque (6mN·m) of the water wheel (total mass of 100 g) rotating at 500 rpm. The transmission between water wheel and EMG is achieved by shaft and sleeve. Details of the mechanical transmission and the V_{oc}/I_{sc} of EMG at 500 rpm could be found in Fig. S3 in the Supporting information. The ww-TENG and EMG were used to charge a 10 μF capacitor and the charging circuit could be seen in the inset image of Fig. 8a, where the ww-TENG and EMG were separately connected with a full wave rectifier and a switch. When the capacitor is purely charged by the ww-TENG, switch S1 should be closed and S2 remains open. Vice versa, when the capacitor is purely charged by the EMG, S2 should be closed and keep S1 open. A combined charging system could be achieved if both S1 and S2 are closed. 500 rpm rotating speed is employed during the charging process which corresponds to a linear flow velocity of 2.6 m/s. This linear velocity is closed to the speed of the narrow reaches. The charging curves of using ww-TENG, EMG, and the combined system are shown in Fig. 8a. It is seen that the capacitor could be charged to over 16 V by pure ww-TENG with a duration of 250 s. At the same rotating speed of 500 rpm and same duration of 250 s, the 10 μF capacitor could only be charged to 2.7 V by EMG. This is because that the EMG typically generates a large current but a relatively low voltage [13]. The combined charging system could reach ~ 19 V during 250 s. With the charged capacitor at 16 V by pure ww-TENG device, a commercial LED light bulb is connected to the circuit as shown in the inset of Fig. 8b. Open switch S1 and connect switch S3, the LED light bulb could be lighted up by the charged capacitor. The output power of the ww-TENG is tested as a function of external load resistance (varying from 100 kΩ to 1 GΩ). As shown in Fig. 8b, the maximum average peak power was measured at 5.3 μW when the load resistance is 50 MΩ. It should be noted that the average peak power is obtained by a single unit of the water wheel with a total electrode size of 280 mm × 25 mm. The performance of the EMG is also evaluated at a rotating speed of 500 rpm with varied external load resistance. As shown in Fig. 8b, the EMG presents a high peak power when the load resistance is smaller than 100 kΩ, which is different from the ww-TENG (50 MΩ). This implies that the EMG is more suitable for the applications with a low load resistance, while the ww-TENG is proper for the applications with large load resistance like electrostatic systems. A longevity test was conducted on the ww-TENG for one hour and the result could be found in Fig. S4 in the Supporting information. No obvious degradation on the output current was observed during the longevity test. The short-circuit current returns to zero immediately when the rotation of ww-TENG is shut-off.

4. Conclusions

This study proposed a sliding freestanding TENG based energy harvesting water wheel for power generation using the low speed flowing river. With the rotating motion driven by the paddles of the ww-TENG as well as the flow river, an AC type signal could be detected. The signal is dependent on the length of the electrode: for a pair of short electrodes, there is a zero output signal region, which is caused by the gaps between the two electrodes. A pair of larger electrodes could reduce the zero output signal zone. With the increase of rotating speed, the average peak current increases. However, due to the existence of the adhesion force, the water adhered to the f-ITO electrodes reduces the average peak current. When the rotating speed increases to 300 rpm (linear velocity 1.575 m/s), the performance of f-ITO electrodes starts decreasing. In order to eliminate the effect caused by the water adhered to the ww-TENG, a pair of conformal fluorine coated carbon paper electrodes were prepared. The f-CP electrodes possess a

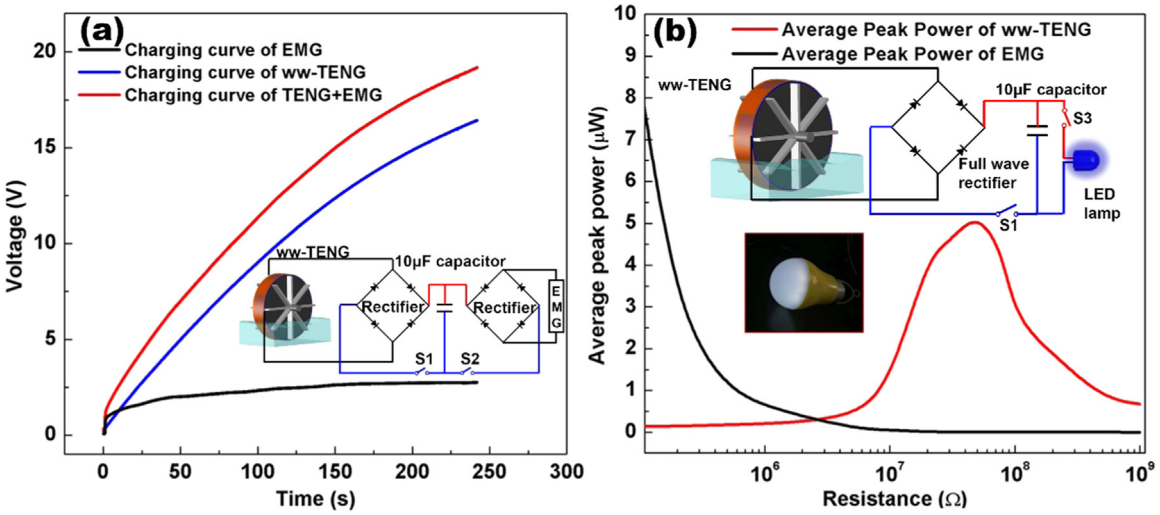

Fig. 8. (a) Charging curves of ww-TENG, a commercial EMG and the combined ww-TENG and EMG system on a 10μF capacitor, inset of (a) shows the circuit of the ww-TENG charging a capacitor. (b) Average peak power of ww-TENG and EMG varying with resistances from 100 kΩ to 1 GΩ. Inset presents the circuit of using the charged capacitor to light up a commercial LED lamp.

superhydrophobic property with a static contact angle of 153°. The water dynamics was analyzed with an adhesion force model and FEA simulation. The results matched well with experimental test. Such a low surface energy enables a fast separation between water and ww-TENG surface and ensures a high current output when the rotating speed is over 300 rpm. The increase of inorganic ion concentrations would reduce the average peak current of the presented ww-TENG. Low pH environment with high H^+ concentration also weaken the output performance. The presented ww-TENG presents a peak power of 5.3 μW when the load resistance is 50 MΩ. With a full wave rectifier, the ww-TENG charged a 10 μF capacitor and lighted up a LED bulb.

Appendix A. Supporting information

Supplementary data associated with this article can be found in the online version at doi:10.1016/j.nanoen.2019.01.083.

References

[1] P.-L. Viollet, From the water wheel to turbines and hydroelectricity. Technological evolution and revolutions, C.R. Mécanique 345 (2017) 570–580.
[2] Ö. Wikander, Archaeological evidence for early water-mills. An interim report, Hist. Technol. 10 (1985) 151–179.
[3] O. Wikander, Handbook of Ancient Water Technology, Brill, Leiden, 2000, p. 741 (ISBN).
[4] Z. Chen, D. Chen, K. Xu, Y. Zhao, T. Wei, J. Chen, et al., Acoustic Doppler current profiler surveys along the Yangtze River, Geomorphology 85 (2007) 155–165.
[5] B. Heidelberg, Carbon and nutrient fluxes in continental margins, Glob. Change – IGBP 10 (2010) 76–80.
[6] T. Nihei, A. Kimizu, Y. Yamasaki, K. Sato, J.H.W. Lee, K.M. Lam, Evaluation of river velocity and discharge with a new assimilated method, Int. J. River Basin Manag. 4 (2006) 27–30.
[7] F.-R. Fan, Z.-Q. Tian, Z.L. Wang, Flexible triboelectric generator, Nano Energy 1 (2012) 328–334.
[8] S. Wang, L. Lin, Z.L. Wang, Nanoscale triboelectric-effect-enabled energy conversion for sustainably powering portable electronics, Nano Lett. 12 (2012) 6339–6346.
[9] Z.L. Wang, Triboelectric nanogenerators as new energy technology for self-powered systems and as active mechanical and chemical sensors, ACS Nano 7 (2013) 9533–9557.
[10] Z.L. Wang, On Maxwell's displacement current for energy and sensors: the origin of nanogenerators, Mater. Today 20 (2017) 74–82.
[11] M. Xu, T. Zhao, C. Wang, S.L. Zhang, Z. Li, X. Pan, et al., High power density tower-like triboelectric nanogenerator for harvesting arbitrary directional water wave energy, ACS Nano (2019).
[12] S.L. Zhang, M. Xu, C. Zhang, Y.C. Wang, H. Zou, H. Xu, et al., Rationally designed sea snake structure based triboelectric nanogenerators for effectively and efficiently harvesting ocean wave energy with minimized water screening effect, Nano Energy 48 (2018) (S2211285518302039).
[13] Y. Zi, H. Guo, Z. Wen, M.H. Yeh, C. Hu, Z.L. Wang, "Harvesting low-frequency (< 5 Hz) irregular mechanical energy: a possible killer application of triboelectric nanogenerator, ACS Nano 10 (2016) 4797–4805.
[14] P. Cheng, H. Guo, Z. Wen, C. Zhang, X. Yin, X. Li, et al., Largely enhanced triboelectric nanogenerator for efficient harvesting of water wave energy by soft contacted structure, Nano Energy 57 (2019) 432–439.
[15] P. Cheng, Y. Liu, Z. Wen, H. Shao, A. Wei, X. Xie, et al., Atmospheric pressure difference driven triboelectric nanogenerator for efficiently harvesting ocean wave energy, Nano Energy 54 (2018) 156–162.
[16] H. Shao, P. Cheng, R. Chen, L. Xie, N. Sun, Q. Shen, et al., Triboelectric-electromagnetic hybrid generator for harvesting blue energy, Nanomicro Lett. 10 (2018) 54.
[17] Y. Xie, H. Zhang, G. Yao, S.A. Khan, M. Gao, Y. Su, et al., Intelligent sensing system based on hybrid nanogenerator by harvesting multiple clean energy, Adv. Eng. Mater. 20 (2018) 1700886.
[18] J. Chen, H. Guo, G. Liu, X. Wang, Y. Xi, M.S. Javed, et al., A fully-packaged and robust hybridized generator for harvesting vertical rotation energy in broad frequency band and building up self-powered wireless systems, Nano Energy 33 (2017) 508–514.
[19] Z.H. Lin, G. Cheng, S. Lee, K.C. Pradel, Z.L. Wang, Harvesting water drop energy by a sequential contact-electrification and electrostatic-induction process, Adv. Mater. 26 (2014) 4690–4696.
[20] S.H. Kwon, J. Park, W.K. Kim, Y.J. Yang, E. Lee, C.J. Han, et al., An effective energy harvesting method from a natural water motion active transducer, Energy Environ. Sci. 7 (2014) 3279–3283.
[21] L.E. Helseth, X.D. Guo, Hydrophobic polymer covered by a grating electrode for converting the mechanical energy of water droplets into electrical energy, Smart Mater. Struct. 25 (2016) 045007.
[22] G. Zhu, Y. Su, P. Bai, J. Chen, Q. Jing, W. Yang, et al., Harvesting water wave energy by asymmetric screening of electrostatic charges on a nanostructured hydrophobic thin-film surface, ACS Nano 8 (2014) 6031.
[23] Y. Su, X. Wen, G. Zhu, J. Yang, J. Chen, P. Bai, et al., Hybrid triboelectric nanogenerator for harvesting water wave energy and as a self-powered distress signal emitter, Nano Energy 9 (2014) 186–195.
[24] Z.L. Wang, T. Jiang, L. Xu, Toward the blue energy dream by triboelectric nanogenerator networks, Nano Energy 39 (2017) 9–23.
[25] Y. Xi, H. Guo, Y. Zi, X. Li, J. Wang, J. Deng, et al., Multifunctional TENG for blue energy scavenging and self-powered wind-speed sensor, Adv. Energy Mater. 7 (2017) 1602397.
[26] T. Jiang, Y. Yao, L. Xu, L. Zhang, T. Xiao, Z.L. Wang, Spring-assisted triboelectric nanogenerator for efficiently harvesting water wave energy, Nano Energy 31 (2017) 560–567.
[27] Z.L. Wang, Catch wave power in floating nets, Nature 542 (2017) 159–160.
[28] T. Kim, J. Chung, D.Y. Kim, J.H. Moon, S. Lee, M. Cho, et al., Design and optimization of rotating triboelectric nanogenerator by water electrification and inertia, Nano Energy 27 (2016) 340–351.
[29] G. Chen, X. Liu, S. Li, M. Dong, D. Jiang, A droplet energy harvesting and actuation system for self-powered digital microfluidics, Lab Chip 18 (2018) 1026.
[30] J. Nie, X. Chen, Z.L. Wang, Electrically responsive materials and devices directly driven by the high voltage of triboelectric nanogenerators, Adv. Funct. Mater. (2018) 1806351.
[31] T. Kim, D.Y. Kim, J. Yun, B. Kim, S.H. Lee, D. Kim, et al., Direct-current triboelectric nanogenerator via water electrification and phase control, Nano Energy 52 (2018) 95–104.
[32] G. Cheng, Z.H. Lin, Z.L. Du, Z.L. Wang, Simultaneously harvesting electrostatic and mechanical energies from flowing water by a hybridized triboelectric nanogenerator, ACS Nano 8 (2014) 1932–1939.
[33] M. Xu, S. Wang, S.L. Zhang, W. Ding, P.T. Kien, C. Wang, et al., A highly-sensitive wave sensor based on liquid-solid interfacing triboelectric nanogenerator for smart marine equipment, Nano Energy 57 (2019) 574–580.
[34] Z. He, Y. Jiang, Y. Li, J. Zhu, H. Zhou, W. Meng, et al., Carbon layer-exfoliated, wettability-enhanced, SO3H-functionalized carbon paper: a superior positive electrode for vanadium redox flow battery, Carbon 127 (2018) 297–304.
[35] J.-G. Wang, H. Sun, H. Liu, D. Jin, R. Zhou, B. Wei, Edge-oriented SnS2 nanosheet arrays on carbon paper as advanced binder-free anodes for Li-ion and Na-ion batteries, J. Mater. Chem. A 5 (2017) 23115–23122.
[36] C. Zhou, Y. Yang, N. Sun, Z. Wen, P. Cheng, X. Xie, et al., Flexible self-charging power units for portable electronics based on folded carbon paper, Nano Res. 11 (2018) 4313–4322.
[37] P. Wang, T. Zhao, R. Bian, G. Wang, H. Liu, Robust superhydrophobic carbon nanotube film with lotus leaf mimetic multiscale hierarchical structures, ACS Nano 11 (2017).
[38] A.I. ElSherbini, A.M. Jacobi, Retention forces and contact angles for critical liquid drops on non-horizontal surfaces, J. Colloid Interface Sci. 299 (2006) 841–849 (Jul 15).
[39] J.H. Snoeijer, B. Andreotti, Moving contact lines: scales, regimes, and dynamical transitions, Annu. Rev. Fluid Mech. 45 (2013) 269–292.
[40] N. Gao, F. Geyer, D.W. Pilat, S. Wooh, D. Vollmer, H.-J. Butt, et al., How drops start sliding over solid surfaces, Nat. Phys. 14 (2017) 191–196.
[41] B. Müller, M. Berg, B. Pernet-Coudrier, W. Qi, H. Liu, The geochemistry of the Yangtze River: seasonality of concentrations and temporal trends of chemical loads, Global Biogeochem. Cycles 26 (2012) (n/a-n/a).
[42] Y. Sun, X. Huang, S. Soh, Using the gravitational energy of water to generate power by separation of charge at interfaces, Chem. Sci. 6 (2015) 3347–3353 (Jun 1).
[43] H.L. Cupples, The surface tensions of calcium chloride solutions at 25° measured by their maximum bubble pressures, J. Am. Chem. Soc. (1945) 987–990.
[44] P. Lun, J. Wang, P. Wang, R. Gao, Y.C. Wang, X. Zhang, et al., Liquid-FEP-based U-tube triboelectric nanogenerator for harvesting water-wave energy, Nano Res. (2018) 1–12.
[45] D.C. Bao, T. Wei, C. He, J. Tao, X. Liang, P.Z. Lai, et al., Ultrafine capillary-tube triboelectric nanogenerator as active sensor for microliquid biological and chemical sensing, Adv. Mater. Technol. 3 (2017).
[46] Y. Qiao, J. Feng, X. Liu, W. Wang, P. Zhang, L. Zhu, Surface water pH variations and trends in China from 2004 to 2014, Environ. Monit. Assess. 188 (2016) 443.
[47] Y. Wu, Y. Su, J. Bai, G. Zhu, X. Zhang, Z. Li, et al., A self-powered triboelectric nanosensor for pH detection, J. Nanomater. 2016 (2016) 1.

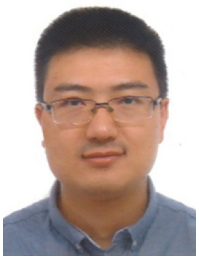

Dongyue Jiang received his Ph.D degree in National University of Singapore. Now he is an Associate Professor at Dalian University of Technology. His research interests include: triboelectric nanogenerators, droplet dynamics as well as their applications in renewable and sustainable systems.

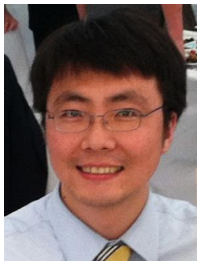

Fei Guo received high Ph.D degree in School of Engineering, Brown University. Now he is a Full Professor in Dalian University of Technology. His research interests include thermal engineering, chemical engineering and material science.

Minyi Xu received his Ph.D degree from Peking University. Now he is an Associate Professor in Dalian Maritime University. His research interests include water wave related TENG devices in applications such as intelligent shipping and so on.

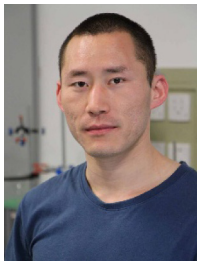

Jingcheng Cai is a Ph.D candidate under supervision of Prof. Fei Guo, he is currently working on the membrane with different hydrophobicity for desalination applications.

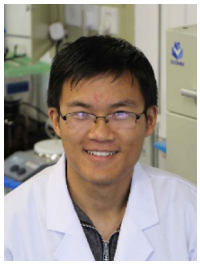

Shuo Cong is a Ph.D candidate under supervision of Prof. Fei Guo and he is working on the modified ceramic tube desalinations.

Ming Jia received his Ph.D degree from Dailian University of Technology. Now he is a Full Professor at Dalian University of Technology. His research interests includes numerical modelling of fluid flow and combustion systems, high speed imaging.

Guijun Chen is an Associate Professor in Dalian University of Technology. He is working on the modelling and analysis of thermal energy systems hydrodynamics including boilers, heat exchangers, recycling of condensate water and so on.

Yongchen Song is a Full Professor, vice President of Dalian University of Technology, Director of Key Laboratory of Ocean Energy Utilization and Energy Conservation of Ministry of Education. His research interests includes Methane hydrate and ocean energy utilization.